

On the ballistic transport in nanometer-scaled double-gate MOSFET

Jérôme Saint Martin, Arnaud Bournel, Philippe Dollfus

*Institut d'Electronique Fondamentale, CNRS UMR 8622, Université Paris Sud, Bât. 220,
F-91405 Orsay cedex, France*

Corresponding author

Jérôme Saint Martin

Institut d'Electronique Fondamentale

CNRS UMR 8622, Université Paris Sud, Bât. 220

F-91405 Orsay cedex, France

Tel.: 33 1 69 15 40 37, Fax: 33 1 69 15 40 20, E-mail: stmartin@ief.u-psud.fr

Abstract

The scattering effects are studied in nanometer-scaled double-gate MOSFET, using Monte Carlo simulation. The non-equilibrium transport in the channel is analyzed with the help of the spectroscopy of the number of scatterings experienced by electrons. We show that the number of ballistic electrons at the drain-end, even in terms of flux, is not the only relevant characteristic of ballistic transport. Then the drive current in the 15 nm-long channel transistor generations should be very close to the value obtained in the ballistic limit even if all electrons are not ballistic. Moreover, in accordance with the conventional believe, we put in evidence that the majority of back-scattering events take place in the first half of the channel, but the contribution of the second half to the drive current can not be considered as negligible in any studied case.

Keywords

Silicon, SOI, MOS devices, MOSFETs, nanotechnology, semiconductor device modeling, Monte Carlo methods, backscattering, ballistic transport.

1 Introduction

Double-gate MOSFET architecture (DGMOS) is a potential solution to overcome short channel effects in the 65 nm ITRS node [1], that is for physical gate lengths smaller than 25 nm. In such nano-transistors where the channel length is comparable to the electron mean free path, non stationary [2] or even ballistic [3] transport is probably of great importance regarding the device performance. This question is however rather controversial from a theoretical point of view.

According to Natori prediction [4], non stationary transport in ultra-small devices, and thus statistical fluctuation of random scattering events undergone by charge carriers in the channel, should lead to dramatic time fluctuations of drive current. After Monte Carlo simulation results, small variations in the number and the position of doping atoms in the channel of a 50 nm bulk MOSFET significantly influence the transport properties and the drain current [5]. Ballistic transport in undoped channel may be the solution to limit these types of fluctuations.

Lundstrom and coworkers have studied in detail the influence of the ballistic transport in such devices on the drain current [6],[7]. They developed models describing nano-DGMOS operating in the ballistic or quasi-ballistic limit. These models are based on the concept of thermionic injection from source-end into the channel. According to such approach, the electron velocity at the source-end, and thus the drive current, should be limited by the "source-to-channel" energy barrier and by back-scatterings in the low-field region, i.e. in the vicinity of the barrier.

Svizhenko and Anantram have also investigated the role of scatterings in nanometer-scaled DGMOS [8]. Using a Green-function approach, they show that scatterings at both source- and drain-end influence significantly the drain current.

More recently, Mouis and Barraud [9] have used the Monte Carlo simulation software MONACO, developed in our group, to discuss the evolution of the velocity distribution along the channel of a DGMOS. Their results seem to be in accordance with the thermionic injection mechanism. They also put into evidence the role of doping impurities in the drain contact: some electrons can be reflected towards the channel after having experienced Coulomb interactions in the highly doped drain region, limiting then the velocity in the channel.

To analyze more in detail the transport in nanometer-scaled DGMOS, we study in this paper the behavior of electrons injected from the source as a function of the number of scattering events undergone in the channel. We have introduced in the device Monte Carlo simulator a procedure which allows us to get accurate information on the number of scattering events experienced by each electron during its travel between the source-end and the drain-end of the channel. We can also extract at many positions in the channel the number of back-scattered electrons and the velocity

distributions of electrons having undergone either 0, 1, 2, ... or N scattering events. We thus have relevant information to investigate in detail in this paper the notion of ballisticity [6] and to discuss the actual influence of both ballistic and backscattering effects on the device characteristics and performance.

The paper is organized as follows. The simulated devices and the Monte Carlo model are presented in Section 2 and the results are described and discussed in section 3. First, we analyze the electron transport in the channel by highlighting the ballistic and quasi-ballistic phenomena. Then the influence of the ballisticity on drive current is evaluated. Finally, we investigate the effects of backscattering by emphasizing the actual location and influence of back-scattering events.

2 Model and simulated devices

The simulated DGMOS devices, described in Fig. 1, have effective channel lengths L_{ch} equal to 10 nm, 15 nm, 25 nm or 50 nm and respectively gate lengths L_G equal to 10, 25, 25 and 50 nm. However, the study is focused on 15 nm-and 25 nm-effective channel lengths. The SiO_2 gate oxide T_{ox} and Si body thicknesses T_{Si} are equal to 1.2 nm and 10 nm, respectively. The doping density is $N_D = 5 \times 10^{19} \text{ cm}^{-3}$ in N^+ S-D regions and $N_A = 2 \times 10^{15} \text{ cm}^{-3}$ in the body (P type). The N^+ doping level is relatively low, and may induce a significant series resistance, but it is a realistic value considering the difficulty of electrically activating dopants in such thin body. The N^+/P junctions are assumed to be abrupt. The work function of the gate material is 4.46 eV to achieve the theoretical threshold voltage V_T of 0.2 V. The power supply voltage V_{DD} is fixed at 0.7 V to abide by the 2007 ITRS prediction.

The particle Monte Carlo algorithm is self-consistently coupled with a 2D Poisson solver. The Poisson's equation is solved at each time step equal to 0.1 fs with standard boundary conditions [10]. The number of simulated particles is typically 50000. The simulator does not include quantum confinement effects but allows the careful analysis of scattering effects. The scattering mechanisms included in the simulation are phonon scattering, impurity scattering and surface roughness scattering. The acoustic intra-valley phonon scattering is treated as an elastic process and the intervalley phonon transitions, consisting of three f-type and three g-type processes, are considered via either zeroth-order or first-order transition matrix in agreement with selection rules [11]. The phonon coupling constants given in [10] are used. The impurity scattering rate is derived from the screened Coulomb potential with the momentum-dependent screening length given in [12]. The surface roughness scattering is treated with an empirical combination of diffusive and specular reflections which correctly reproduces the experimental universal mobility curve [13],[14]. Unless

otherwise indicated we have considered in this work a fraction of diffusive reflections C_{diff} equal to 0.14.

The originality of the present work lies in the spectroscopy of the number of scattering events undergone by electrons crossing the active part of the channel (or any predefined part of the device) and in the detailed study of the velocity spectra of different electron populations. Practically, a scattering counting region is predefined with an entrance surface and an exit surface. Typically, the entrance surface is defined either at the source/channel junction or at the position of the top of the gate-induced potential barrier, and the exit surface is placed at the channel/drain junction. Each electron entering the counting region by the entrance surface is flagged and while it remains inside this region the number of scattering events undergone is recorded. At the exit surface we can thus separate electrons into different groups, corresponding to ballistic electrons, once-scattered electrons, twice-scattered electrons, ... N -times scattered electrons, respectively. Of course these groups can be enumerated. Additionally, for each of these groups the energy and velocity spectra are recorded. Such spectra may be also obtained at intermediate surfaces defined all along the counting region, i.e. the channel. It should be noted that these spectra only include electrons coming from the entrance surface and not the electrons entering the counting region by the exit surface. The information about back-scattered electrons is obtained separately: if an electron is back-scattered after having crossed the counting region and re-enter this region by the exit surface, its scattering-story is still recorded and the velocity spectra of such electrons are recorded too. Thus, by possibly changing the place of the exit surface, we can have very detailed information on all carriers participating in the source-drain current. It is very useful to quantify and analyze the effects of ballistic, nearly-ballistic and back-scattered electrons.

3 Results

The variations of the drain current I_D as a function of the source-drain voltage V_{DS} obtained in the 15 nm-, 25 nm- and 50 nm-long transistors for $V_{GS} = V_{DD}$ are shown in Fig. 2. For the 15 nm-long channel, the I_{on} current at $V_{DS} = V_{GS} = V_{DD} = 0.7$ V is $2140 \mu\text{A}/\mu\text{m}$. Such a high value is related to the aggressive scaling of the gate length, to the double-gate architecture and to the relatively thick body film ($T_{\text{si}} = 10$ nm). The drain conductance, and more generally the short channel effects (SCE), are however rather strong in the 15 nm-long channel, as a consequence of the non optimized body thickness. The 25 nm-long channel, better designed, is less sensitive to SCE while keeping I_{on} -value ($1600 \mu\text{A}/\mu\text{m}$) higher than the ITRS Roadmap specification that is $900 \mu\text{A}/\mu\text{m}$. We now examine the transport in these devices biased in the "on-state", i.e. with $V_{GS} = V_{DS} = V_{DD}$.

3.1 From non stationary to ballistic transport

The electron velocity profile along the 15, 25 and 50 nm channels is drawn in Fig. 3. In the 50 nm-long channel, a linear increase of the velocity as a function of the distance is observed in the low field region, that is between about $x = 5$ nm and 20 nm. This behavior reflects a mobility-like regime. On the contrary, in shorter channels the velocity rapidly overshoots the bulk saturation value (10^7 cm/s) in the vicinity of the source-end of the channel, at about $x = 2$ nm for 15 nm-long channel and about $x = 5$ nm for 25 nm-long. This position is near the top of the energy barrier in the conduction band profile, as shown in Fig. 4 for the 15 nm device. Furthermore, a significant velocity value is reached in the source region as a consequence of the relatively low doping level in this N^+ region, which induces a non negligible electric field.

In order to investigate such a non-stationary transport, we plot in Fig. 5 the evolution of the velocity spectra of electrons along the 15 nm-long channel in the first sheets of cells under the front oxide, i.e. between $y = 0$ and $y = 1$ nm (cf. Fig. 1), i.e. at the Si/SiO₂ interface. The transport is stationary in the highly doped source well, as illustrated by the quasi-Gaussian shape of the velocity distribution in the middle of this region. Other spectra are taken in the channel and only concern electrons injected by the source into the channel, excluding those which have been injected or re-injected from the drain. These spectra are very different from stationary ones. In the vicinity of the top of the barrier ($x = 2$ nm), the spectrum is quite similar to a hemi-Gaussian distribution. However electrons with a negative velocity have not completely disappeared. Thus, the regime of pure thermionic injection in the channel is almost but not completely reached in this structure. At a position $x = 4$ nm after the source/channel junction, two separate distributions appear in the velocity spectrum. We can distinguish two peaks corresponding to electrons with either a transverse or a longitudinal effective mass along the source to drain direction. For greater distance x , we observe the propagation of these two distributions along the channel, each one at its own velocity. The electron density decreases as the average velocity increases to satisfy the current conservation and the distributions become narrower and narrower.

At the drain-end of the 15 nm-long device, the velocity spectrum of electrons injected from the source calculated at the Si/SiO₂ interface looks like two very well-defined peaks as shown in Fig. 6. According to energy conservation between the barrier region and the drain-end of the channel, it is easily demonstrated that the peak velocity values in Fig. 6 correspond to ballistic electrons flowing from source to drain with a transverse ($m_t = 0.19 m_0$ where m_0 is the free electron mass) or a longitudinal ($m_l = 0.916 m_0$) effective mass (this calculation method is described in [8] and [10]). In Fig. 6, the spectrum of electrons injected from the drain at $x = 15$ nm is also plotted in dotted line. The distribution of these electrons is made up of the sum of two nearly Gaussian distributions.

These distributions have different standard deviations: the widest corresponds to electrons with a transverse mass and the other are to electrons with a longitudinal mass. Average velocities of these distributions tend to zero; therefore the net contribution of drain-injected electrons to the current at the drain-end is weak. However, according to Fig. 6 the number of electrons, at the drain-end coming from the drain is the greatest, which certainly influences the potential distribution.

Thus, to get a complete description of all electron populations present in the channel, we have to compare Fig. 5 with Fig. 7 where the evolution along the channel of velocity spectra of electrons injected from drain is plotted. First we can notice on this Fig. 7 that the number of “drain injected” electrons decreases during their propagation from drain to source. The general shape of those spectra, i.e. with distinctive “transverse” and “longitudinal” Gaussian distributions, is conserved along the channel at $x = 15$ nm, 12 nm and 4 nm. Moreover, for drain injected carriers crossing the top of the barrier, a thermionic behavior is observed at $x = 1$ nm and 0 nm. Indeed, the part with a positive velocity of “drain injected” electron distribution decreases abruptly and tends to a hemi-Gaussian distribution. Then even if the number of electrons injected from the drain near the source-end at $x = 1$ nm is weak, they represent 1.7% of the “source injected” at the same abscise electrons (cf. Fig. 5), but they have a very negative mean velocity, $\langle v_x \rangle = -0.77 \times 10^7$ cm/s comparable with the mean “source” electron velocity, that is 0.85×10^7 cm/s. Then their influence on drive current is not completely negligible in this structure.

3.2 Influence of the ballisticity on drive current

Those first analyses of velocity evolution along the channel indicate clearly that the transport is completely out of equilibrium. Furthermore, the velocity spectrum of “source-injected” electrons at the drain-end (Fig. 6) suggests that ballistic electrons have an important role in the transport for nanometer-scaled DGMOS devices. To try to get a more quantitative insight into ballistic and/or quasi-ballistic transport, we present a new kind of analysis which allows dissecting the velocity spectra presented in Fig. 6.

The Fig. 8 represents the velocity distributions calculated at the drain-end of the 15 nm-long channel device for electrons flowing from the source by undergoing 2, 1 or 0 scattering events. Contrary to the spectra presented above (i.e. in Fig. 5, Fig. 6 and Fig. 7) calculated at the Si/SiO₂ interface, these new distributions are calculated on the full body thickness, i.e. between $y = 0$ and $y = T_{\text{Si}}$ (cf. Fig. 1). A 2D effect is clearly observed in Fig. 8: the ballistic peaks are wider than those presented in Fig. 6 as they result from the sum of peaks with different maxima. Indeed, as shown in Fig. 4, the potential drop varies as a function of the channel depth, i.e. along the y -axis (cf. Fig. 1), which makes the ballistic peak position dependant on y . For instance, according to the potential

drop plotted in Fig. 4, the transverse mass peak velocity equals 6.5×10^7 cm/s at $y = 0$ nm and 7.0×10^7 cm/s at $y = T_{si}/2$. We also verify that the distribution tails observed in Fig. 6 are caused by electrons having undergone interactions during their channel crossing. Moreover, we notice that the shapes of the quasi-ballistic velocity spectra, i.e. the spectra obtained for electrons which have undergone 1 or 2 interactions, is closer to that of a ballistic spectrum than to stationary one. This suggests that devices can drive on-currents I_{on} very close to the limit value obtained for a ballistic channel, even if all the electrons are not purely ballistic at the drain-end.

The Fig. 9 represents the same kind of velocity distributions for “source injected” electrons but calculated near the top of the barrier, i.e. at $x = 3$ nm from the source-end. Ballistic electrons represent here 72% of the total “source injected” electron population. As expected, we can verify that ballistic electrons are thermionically injected as their velocity spectrum looks like a hemi-Gaussian distribution. Nevertheless electrons which have already been scattered exist and are not negligible in comparison with the ballistic electron population (28%). The negative part of their distribution is almost as important as the positive part. The mean velocity of scattered electrons thus tends to zero and their contribution to the current is negligible. Therefore, drain-injected carriers excepted, the current transport is nearly ballistic at the top of the barrier.

In this connection, we have defined a counting region by an entrance surface and an exit surface located at the source/channel and channel/drain junctions, respectively. The numbers of scattering events N_{scatt} experienced by each carrier crossing this country region, i.e. the channel, is calculated and the electron population exiting the channel at the drain end may be separated in different groups as a function of the number of scatterings N_{scatt} . The fraction of population corresponding to these groups is plotted in Fig. 10 as a function of N_{scatt} for DGMOS of different effective channel length: 15 nm, 25 nm and 50 nm. We have also indicated for comparison, in dotted line, the similar distribution obtained at the drain-end for a conventional 50 nm bulk MOSFET with the following characteristics: a single gate, a channel length $L_{ch} = 50$ nm, an oxide thickness $T_{ox} = 1.2$ nm, a junction depth $X_j = 20$ nm and a highly doped channel $N_A = 10^{18}$ at/cm³. The latter is a bell-curve with a maximum on $N_{scatt} = 5$ which corresponds to the ratio L_{ch}/λ_{eff} where L_{ch} is the effective channel length and λ_{eff} is defined as an effective mean free path. On the contrary, in all lightly-doped DGMOS the group of ballistic electrons corresponds to the higher fraction, but they are majority in the 15 nm-long channel only. This indicates that the effective mean free path λ_{eff} is smaller than the channel length in all DGMOS. However, the fraction of electrons decreases as N_{scatt} (the number of scatterings) increases and the distribution spreads out when L_{ch} increases. For the 15 nm-long channel, the curve is a pure exponential function. In both 50 nm-long channel devices (DGMOS and bulk) the interaction spectrum tends to a more stationary-like one.

From now, we define an intrinsic ballisticity B_{int} which corresponds to the percentage of electrons which are ballistic at the drain-end in Fig. 10 [15]. The line in Fig. 11 is an interpolated curve obtained by linking the intrinsic ballisticity B_{int} at the drain-end for the 3 different DGMOS with channel effective lengths L_{ch} equal to 15 nm, 25 nm and 50 nm and by assuming $B_{\text{int}} = 100\%$ for $L_{\text{ch}} = 0$. The smooth curve obtained with these last 3 DGMOS seems particularly relevant because it gives for $L_{\text{ch}} = 10$ nm the same result as the complete Monte Carlo simulation of a 10 nm-long device (closed circle). From such a semi classical Monte Carlo approach, one can thus estimate that the ballistic electrons should be largely predominant (i.e. with an intrinsic ballisticity B_{int} greater than 90%) only for channel lengths smaller than about 3 nm. However, quantum transport effects have to be considered for investigating L_{ch} -values smaller than 10 nm [7], which may modify this prediction.

To investigate how the intrinsic ballisticity B_{int} at the drain-end is related to the on-current I_{on} , we have artificially modified it from 0 as in full stationary transport to 100% as in pure ballistic transport. We call $I_{\text{on_bal}}$ the on-current obtained for a ballistic channel, that is without any phonon or roughness effects. Then, we study the effective ballisticity B_{eff} , defined as $B_{\text{eff}} = I_{\text{on}}/I_{\text{on_bal}}$ [6], as a function of the intrinsic ballisticity B_{int} at the drain-end.

To this end, we have varied the oxide roughness coefficient C_{diff} and the phonon scattering coefficient. To modify the phonon scattering coefficient, all standard value are multiplied by a coefficient K_{ph} varying from 0 for a ballistic channel, to 20 for a very resistive channel. The evolution of B_{eff} as a function of B_{int} for a given C_{diff} and for different phonon scattering coefficient, i.e. K_{ph} values, is plotted in dotted line in Fig. 12. The results obtained for $C_{\text{diff}} = 1$ (respectively $C_{\text{diff}} = 0.14$) and for $K_{\text{ph}} = 0, 1, 2, 5, 10$ and 20 (respectively $K_{\text{ph}} = 0, 0.5, 1, 2$), is indicated with open squares (respectively closed triangles). The results obtained for various roughness coefficients C_{diff} and for a given phonon coefficient K_{ph} are shown in solid lines: on the one hand for $K_{\text{ph}} = 1$ and $C_{\text{diff}}: 0, 0.07, 0.14, 0.21, 0.4, 0.7$ and 1 (open circles), and, on the other hand, for $K_{\text{ph}} = 0$ with $C_{\text{diff}}: 0, 0.14, 0.5$, and 1 (closed squares).

These results show an overall view of the effect of each kind of interaction. For an intrinsic ballisticity B_{int} greater than 20% the effect of each type of interaction (phonon or roughness scattering) yields a linear behavior $B_{\text{eff}}(B_{\text{int}})$ but with a slope depending on the type of interaction. Below this limit, when the transport is more stationary, the $B_{\text{eff}}(B_{\text{int}})$ relation is no more simply linear. Thus there is neither an equality nor a unique linear relation between the effective ballisticity B_{eff} and the intrinsic ballisticity B_{int} . Thus the effective ballisticity B_{eff} (in terms of current) alone does not provide enough information to quantify accurately the intrinsic ballisticity B_{int} . However, there is no denying that these 2 quantities are strongly correlated. Besides, we notice that the

intrinsic ballisticity B_{int} is always overestimated by the effective ballisticity B_{eff} : for instance $B_{\text{int}} = 52\%$ and $B_{\text{eff}} = 84\%$ for the standard DGMOS ($K_{\text{ph}} = 1$ and $C_{\text{diff}} = 0.14$).

3.3 Back-scattering localization and its effect on the current

To investigate further more the effects of scattering, a flux approach may be used [6]. We have tried to identify the part of the channel giving the highest contribution to back-scattering effect. So, a control volume is defined, as shown in Fig. 13, by an surface entrance and an exit surface which can be moved along the channel. By calculating, the different fluxes: Φ_I^+ , Φ_O^+ , Φ_{II}^- and Φ_{I2}^- , the relevant back-scattering coefficients may be extracted. Fluxes Φ_I^+ and Φ_O^+ , oriented as indicated in Fig. 13, are the ingoing flux at the entrance surface and the outgoing flux at the exit surface, respectively. The flux Φ_{II}^- represents the flux of electrons having entered the control volume by the entrance surface and crossing back the entrance surface without having crossed the exit surface. The flux Φ_{I2}^- represents the flux of electrons which have entered in the control volume by the entrance surface and which cross back the entrance surface after having crossed the exit surface.

The back-scattering coefficient $R(x)$ of the control volume between an entrance surface located about at the top of the barrier and an exit surface located at the distance x from the source end, is equal to $\Phi_{II}^-(x)/\Phi_I^+$. The evolution of $R(x)$ obtained by moving the exit surface along the channel from the top of the barrier to the drain end is plotted in Fig. 14 for 15 nm- and 25 nm-long devices. The maximum back-scattering coefficient R_{max} for the whole structure including the drain contact can be calculated as $R_{\text{max}} = \max[R(x)] = [\Phi_{II}^-(x) + \Phi_{I2}^-(x)]/\Phi_I^+$. First, we remark that at the drain-end the backscattering coefficient $R(L_{\text{ch}})$ is slightly lower than R_{max} . This difference, due to electrons back-scattered in the drain, should be overestimated by a non optimal scattering model in the drain. For instance, the short range electron-electron interactions are not taken into account in our Monte Carlo simulation. Then, we observe a monotonous variation of $R(x)$ along the channel. The increase of $R(x)$ is much more important in the first half part of the channel as the back-scattering events take place mainly there. However this tendency decreases when the effective channel length L_{ch} decreases: $R(x = L_{\text{ch}}/2) = 0.91 \times R(L_{\text{ch}})$ for $L_{\text{ch}} = 25$ nm, while $R(x = L_{\text{ch}}/2) = 0.81 \times R(L_{\text{ch}})$ for $L_{\text{ch}} = 15$ nm. Moreover, in the first part of the channel the increase of $R(x)$ is rather uniform, just a bit faster in the vicinity of the top of the barrier. Thus, it is difficult to accurately define in the first channel half a region having a predominant impact in terms of back-scattering. For instance, trying to evaluate the total back-scattering coefficients $R(L_{\text{ch}})$ or R_{max} with an $R(x)$ corresponding to a low field region extracted from the conduction band, as it is suggested in [6], produces a significant error: at $x = 4$ nm where the potential drop is equal to

50 meV (cf. Fig. 4) which corresponds to twice the 2D thermal energy value ($k_B \times T / q$) at 300 K, $R(x) = 6.5\%$ i.e. $R(x) = 0.56 \times R(L_{ch}) = 0.46 \times R_{max}$.

As we have shown that the scattering events which have a direct impact in terms of current are mainly located in the first channel half, we have tried to confirm that by a direct on-current analysis of new devices with different scattering properties along the channel. Thus, three new 25 nm -long DGMOS structures called ‘bal-bal’, ‘bal-sta’ and ‘sta-bal’ have been simulated. The channel of these DGMOS is divided in 2 equal parts. The term ‘sta’ stands for the channel half having standard scattering properties of Si doped to 2.10^{15} at/cm³: standard phonon scattering coefficient $K_{ph} = 1$ (cf. 3.2) and roughness coefficient $C_{diff} = 0.14$, and ‘bal’ stands for the ballistic channel half (without any scattering: neither phonon $K_{ph} = 0$, nor impurity, nor roughness coefficient $C_{diff} = 0$). So ‘sta-bal’ is a DGMOS with a standard first channel half and a ballistic second channel half.

The Fig. 15, which represents the intrinsic ballisticity B_{int} along the channel, well illustrates the different characteristics of these DGMOS structures. In ‘bal-bal’ the ballisticity remains at 100% all along the channel. In ‘sta-bal’ the ballisticity only decreases in the first channel half. It is the opposite for ‘bal-sta’. Nevertheless in ‘bal-sta’ the ballisticity slightly decreases in the first ballistic channel half due to the contribution of electrons back-scattered from the second standard half.

The Fig. 16 shows on both linear and logarithmic scales the evolution of the drain current I_D as a function of the gate voltage V_{GS} at $V_{DS} = V_{DD}$. First we notice that all devices have the same threshold voltage $V_T \approx 0.3$ V. Moreover, the subthreshold behavior is not degraded by SCE, the subthreshold slope being equal to 70 mV/dec. The characteristics only differ in the transconductance $g_m (= \frac{\partial I_D}{\partial V_{GS}} \Big|_{high V_{GS}})$ above the threshold voltage V_T and, as a consequence, in the on-current I_{on} .

The variations of drain current I_D as a function of source-drain voltage V_{DS} obtained in these DGMOS at $V_{GS} = 0.7$ V are shown in solid lines in Fig. 17. In linear regime, the resistance $R_{on} = \frac{\partial V_{DS}}{\partial I_D} \Big|_{low V_{DS}}$ extracted from Fig. 17 simply follows the Ohm’s law: R_{on} has the same value for ‘bal-sat’ and ‘sta-bal’. It is greater for the standard channel and lower for the ballistic channel. In the saturation regime, with nearly the same drain saturation voltage V_{DSsat} for all devices, the following output conductances $G_D = \frac{\partial I_D}{\partial V_{DS}} \Big|_{V_{GS}=0.7V}$ are extracted at $V_{GS} = 0.7$: $G_{D_BB} = 360 \mu\text{S}/\mu\text{m}$ for ‘bal-bal’, $G_{D_BS} = 340 \mu\text{S}/\mu\text{m}$ for ‘bal-sta’, $G_{D_SB} = 270 \mu\text{S}/\mu\text{m}$ for ‘sta-bal’, $G_{D_SS} = 190 \mu\text{S}/\mu\text{m}$ for ‘standard’. We observe that the more ballistic the channel is, in

particular in its first half, the greater the conductance is. Thus, we deduce that the lack of scattering degrades the saturation behavior.

If each channel part had the same influence on drive current, ‘sta-bal’ and ‘bal-sta’ on current would be equal to the average on-current between ‘standard’ and ‘bal-bal’, i.e. equal to $1980 \mu\text{A}/\mu\text{m}$. As the on-current I_{on} is equal to $2000 \mu\text{A}/\mu\text{m}$ for ‘bal-sta’ and $1850 \mu\text{A}/\mu\text{m}$ for ‘sta-bal’, we deduce that the ballistic channel part location, i.e. the scattering localization, has an influence on the on-current. Moreover, in accordance with the conventional believe, the first channel half has a slightly greater importance than the second half of the channel in terms of back-scattering coefficient and resulting current. However this study also reveals that the second part of the channel keeps nevertheless a significant impact. Indeed the I_{on} current is 15% greater for ‘sta-bal’ than for standard and it is 14% greater for ‘bal-bal’ than ‘bal-sta’.

It should be mentioned that we have obtained similar results for bulk MOSFET of higher channel length, i.e. 50 nm and 180 nm. Low R_{on} , i.e. high channel mobility, is beneficial for the on-current I_{on} , and a low mobility, in particular the first half, is suitable to keep a weak output conductance G_{D} .

4 Conclusion

According to our spectroscopic study of the number of scattering events along the channel, ballistic electrons are indeed of great importance in nanometer-scaled double-gate MOSFET. In nano-DGMOS, the ballistic limit (intrinsic ballisticity $B_{\text{int}} = 100\%$ i.e. 100% of electrons injected from the source are ballistic at the drain-end) is far to be reached for channel lengths larger than 10 nm: the intrinsic ballisticity is about 50% in 15 nm-long channel. However, the drive current I_{on} is closer to the value $I_{\text{on_bal}}$ obtained with a pure ballistic channel: the ratio $I_{\text{on}}/I_{\text{on_bal}}$, i.e. the effective ballisticity B_{eff} , is more than 80%. Then the number of ballistic electrons, even in terms of flux as we defined the intrinsic ballisticity B_{int} , is not the only relevant characteristic of ballistic transport. There even if the “ballistic limit” is still “a mere pipe dream” considering the numerous types of significant interactions in nano-scaled structures [16], the on-current in next transistor generations should be very close to this limit.

Moreover, it is difficult to extract from Monte Carlo results a particularly significant region of the channel which would determine I_{on} . In accordance with the conventional believe, the majority of back-scattering events takes place in the first half of the channel. However, the contribution of the second half can not be considered as negligible in any studied case.

This work is supported by the French RMNT project CMOS-D-ALI and we thank Emile Grémion for his contribution.

References

- [1] International Technology Roadmap for Semiconductors: 2002 Update, <http://public.itrs.net/>
- [2] T. Mizuno and R. Ohba, "Experimental study of nonstationary electron transport in sub-0.1 μm metal-oxide-silicon devices: Velocity overshoot and its degradation mechanism", *J. Appl. Phys.*, vol. 82, pp. 5235-5240, 1997
- [3] S. E. Laux and M. V. Fischetti, "Monte Carlo simulation of submicrometer Si n-MOSFET's at 77 and 300 K", *IEEE Electron Dev. Lett.*, vol. 9, pp 467-469, 1988
- [4] K. Natori, "Ballistic metal-oxide-semiconductor field effect transistor", *J. Appl. Phys.*, vol. 76, pp. 4879-4890, 1994
- [5] P. Dollfus, A. Bournel, S. Galdin, S. Barraud, and P. Hesto, "Effect of discrete impurities on electron transport in ultra-short MOSFET using 3D Monte Carlo simulation", *cond-mat/0310718*
- [6] M. Lundstrom and Z. Ren, "Essential physics of carrier transport in nanoscale MOSFETs", *IEEE Trans. Electron. Dev.*, vol. 49, pp. 133-141, 2002
- [7] J.-H. Rhew, Z. Ren, and M. S. Lundstrom, "A numerical study of ballistic transport in a nanoscale MOSFET", *Solid-State Electron.*, vol. 46, pp. 1899-1906, 2002
- [8] A. Svizhenko and M. P. Anantram, "Role of scattering in nanotransistors", *IEEE Trans. Electron. Dev.*, vol. 50, pp. 1459-1466, 2003
- [9] M. Mouis and S. Barraud, "Velocity distribution of electrons along the channel of nanoscale MOS transistors", in *Proc. ESSDERC 2003*
- [10] P. Dollfus, "Si/Si_{1-x}Ge_x heterostructures: electron transport and field-effect transistor operation using Monte Carlo simulation", *J. Appl. Phys.*, vol. 82, pp. 3911-3916, 1997
- [11] T. Yamada, J. R. Zhou, H. Miyata, and D. K. Ferry, "In-plane transport properties of Si/Si_{1-x}Ge_x structure and its FET performance by computer simulation", *IEEE Trans. Electron Devices*, vol. 41, pp. 1513-1522, 1994
- [12] N. Takimoto, "On the screening of impurity potential by conduction electrons", *J. Phys. Soc. Jpn.*, vol. 14, pp. 1142-1158, 1959
- [13] E. Sangiorgi and M. R. Pinto, "A semi-empirical model of surface scattering for Monte Carlo simulation of silicon n-MOSFET", *IEEE Trans. Electron Devices*, vol. 39, pp. 356-361, 1992
- [14] S. Keith, F. M. Bufler, and B. Meinerzhagen, "Full-band Monte Carlo device simulation of an 0.1 μm n-channel MOSFET in strained silicon material", in *Proc. ESSDERC'97* (Editions Frontières, Paris), 1997, pp. 200-203
- [15] It must be highlighted that the intrinsic ballisticity is a percentage in terms of positive current flux. It does not correspond to an electron population but to an electron population weighted by its velocity. Moreover only electrons with a positive velocity along the source-drain-axis, i.e. the x-axis (cf. Fig. 1), have been considered.
- [16] M. V. Fischetti, "Scaling the MOSFETs to the limit: A physicist's perspective", *International Workshop on Computational Electronics IWCE-9*, 25-28 May 2003, abstract

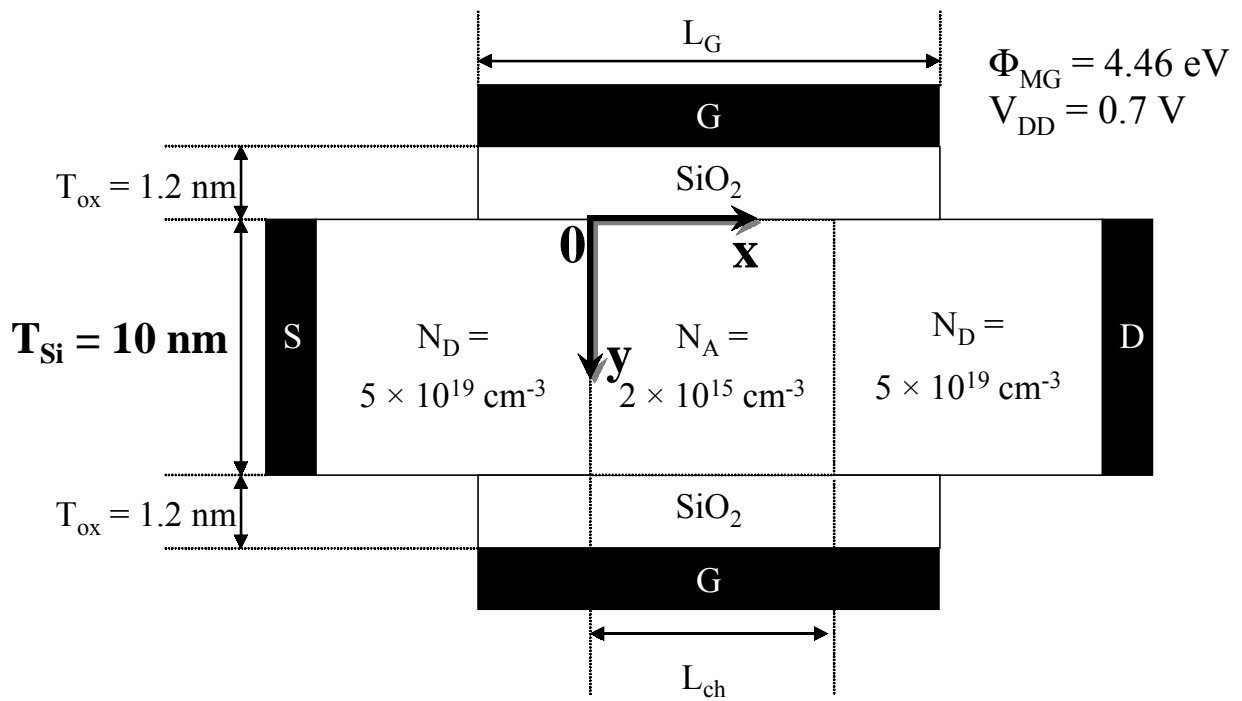


Fig. 1: Schematic of DGMOS structures.

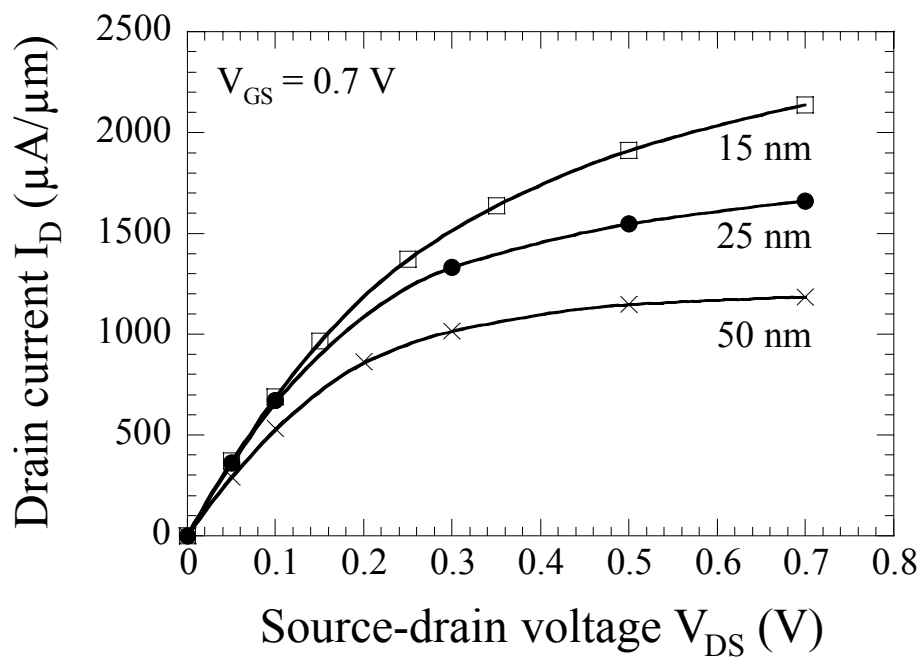


Fig. 2: Drain current I_D versus drain voltage V_{DS} at $V_{GS} = 0.7$ V in DGMOS of different channel lengths L_{ch} . Crosses: $L_{ch} = 50$ nm, closed circles: $L_{ch} = 25$ nm, and open squares: $L_{ch} = 15$ nm.

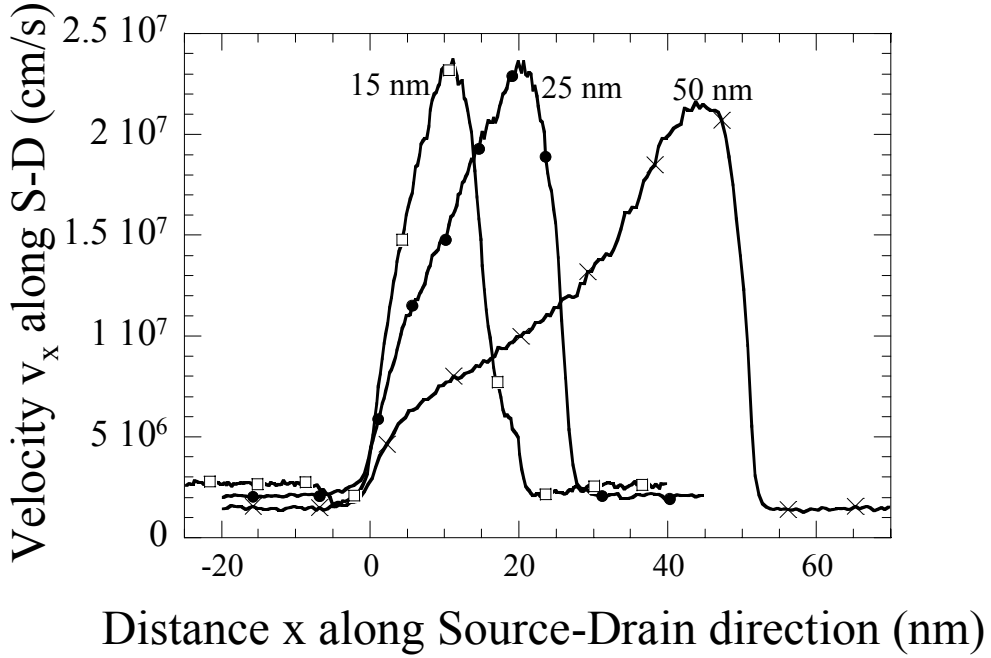


Fig. 3: Electron velocity v_x versus distance x along the S-D direction in DGMOS of different channel lengths at $V_{DS} = 0.7$ V. The velocity v_x is calculated in the first sheets of cells under the front gate i.e. between $y = 0$ and $y = 1$ nm. Crosses: $L_{ch} = 50$ nm, closed circles: $L_{ch} = 25$ nm, and open squares: $L_{ch} = 15$ nm. $x = 0$ corresponds to the position of the source/channel junctions.

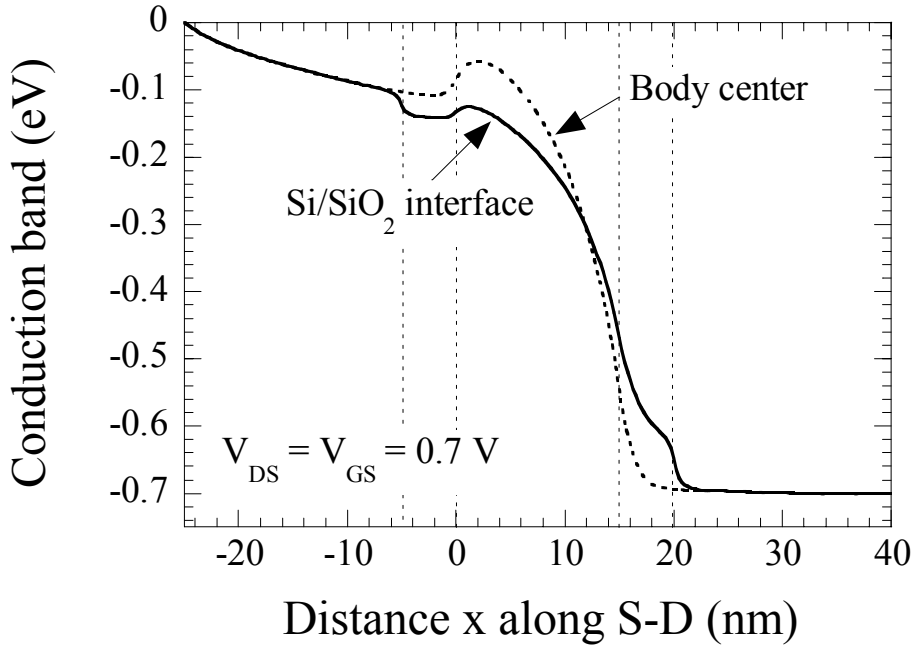


Fig. 4: Conduction band versus distance x along the S-D direction in the on-state ($V_{GS} = V_{DS} = V_{DD}$) for the 15 nm-long transistor: $L_{ch} = 15$ nm and $L_G = 25$ nm for different distances y from the gate: $y = 0$ nm for the Si/SiO₂ interface and $y = T_{Si} / 2$ for the body center. The dotted lines indicate the S-D gate overlap, the x-axis origin being the same as in Fig. 3.

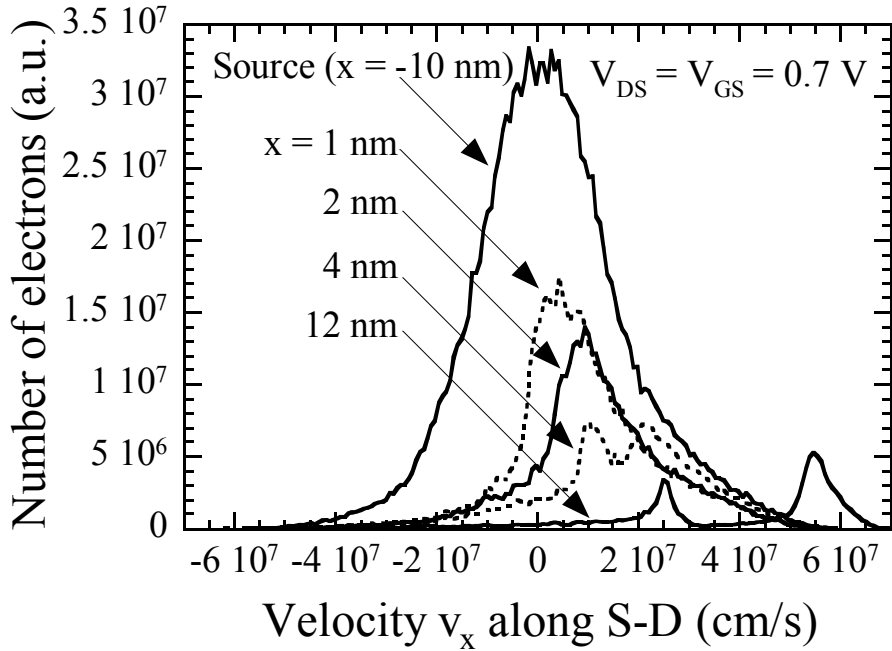


Fig. 5: Velocity v_x distributions calculated in the N^+ source region and at different positions into the 15 nm-long channel. For $x > 0$, only electrons injected from the source are considered.

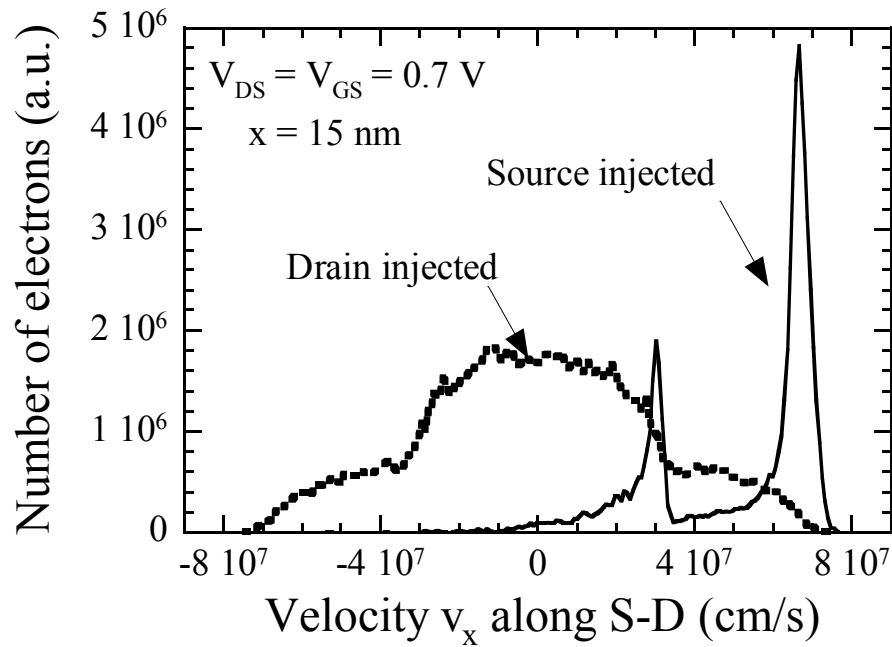


Fig. 6: Velocity v_x distributions of electrons flowing from the source (solid lines) and electrons flowing from the drain (dotted lines) calculated at the drain-end ($x = 15$ nm) of the 15 nm-long channel.

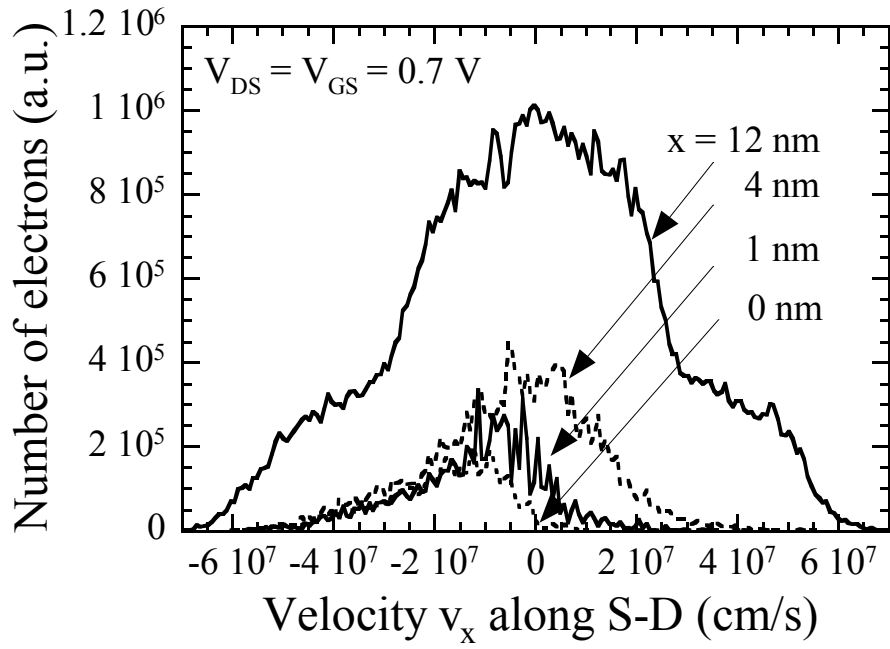


Fig. 7: Velocity v_x distributions calculated at different channel positions for electrons injected by the drain into the 15 nm-long channel.

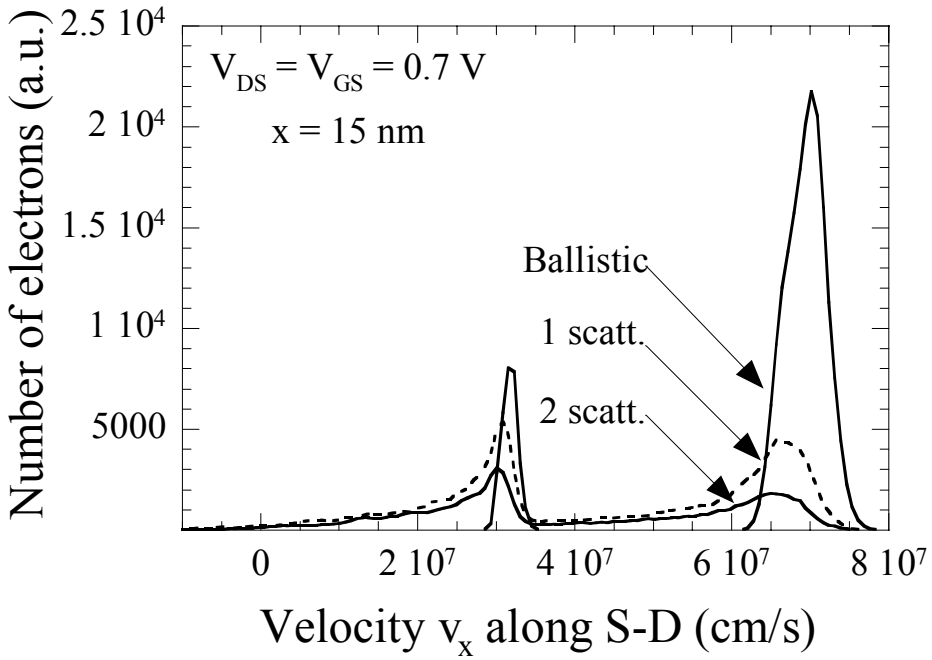


Fig. 8: Velocity v_x distributions calculated at the drain-end ($x = 15$ nm) of the 15 nm-long channel for electrons flowing from the source and undergoing either 2, 1 or 0 scattering events.

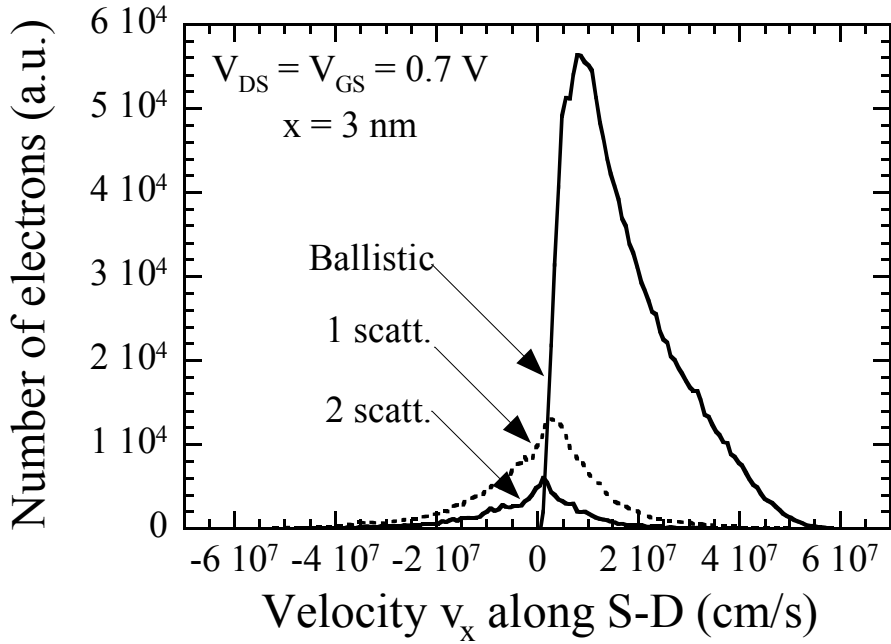


Fig. 9: Velocity v_x distributions calculated at $x = 3$ nm from the source-end of the 15 nm-long channel for electrons flowing from the source, and undergoing either 2, 1 or 0 scattering events.

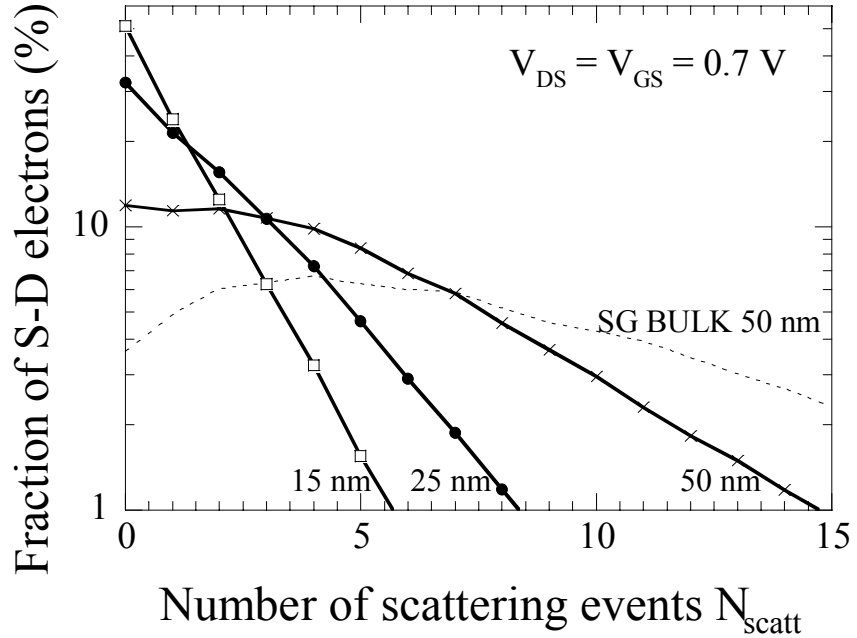


Fig. 10: Fraction of electrons flowing from S to D versus the number of scattering events N_{scatt} undergone during the channel crossing. Conventional bulk MOSFET (Single gate, $L_{ch} = 50$ nm) distribution: dotted line. DGMOS distributions: solid lines. Crosses: $L_{ch} = 50$ nm, closed circles: $L_{ch} = 25$ nm, and open squares: $L_{ch} = 15$ nm

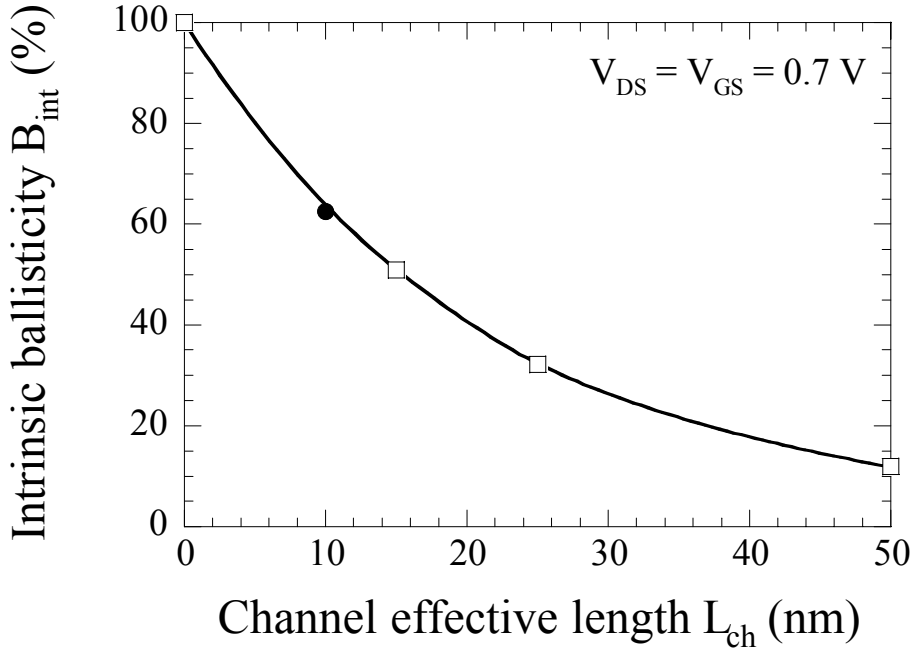


Fig. 11: Intrinsic Ballisticity B_{int} at the drain-end versus channel effective length L_{ch} .

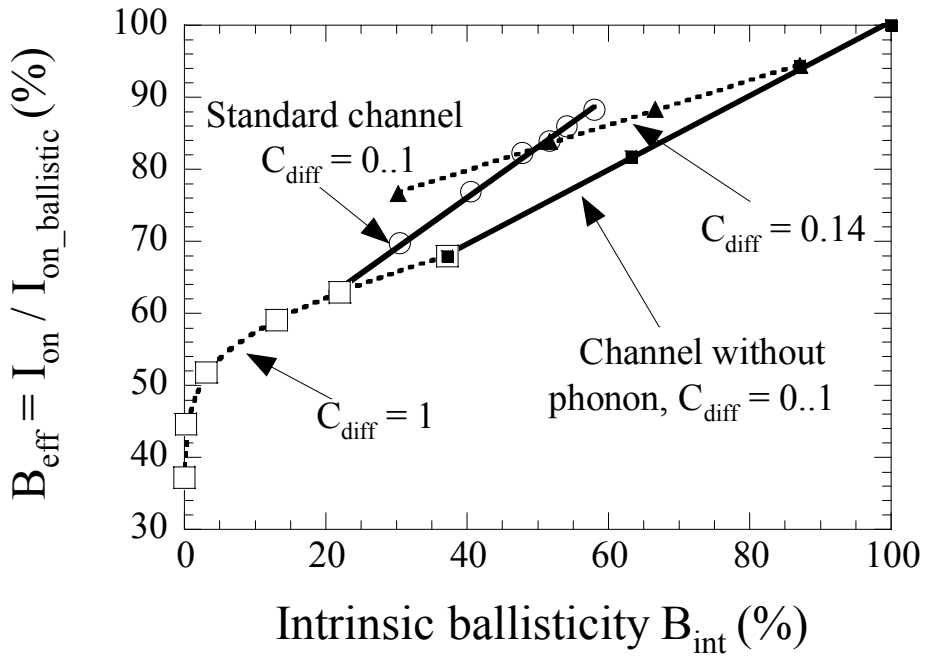


Fig. 12: Effective ballisticity $B_{\text{eff}} = I_{\text{on}} / I_{\text{on_bal}}$ versus intrinsic ballisticity B_{int} in the 15 nm-long device. Results are obtained by varying the intensity of the oxide roughness C_{diff} or the phonons scattering coefficient K_{ph} . For $C_{\text{diff}} = 1$ (respectively $C_{\text{diff}} = 0.14$) and $K_{\text{ph}} = 0, 1, 2, 5, 10$ and 20 (respectively $K_{\text{ph}} = 0, 0.5, 1, 2$): open squares (respectively closed triangles). For $K_{\text{ph}} = 1$ (respectively $K_{\text{ph}} = 0$) and $C_{\text{diff}} = 0, 0.07, 0.14, 0.21, 0.4, 0.7$ and 1 (respectively $C_{\text{diff}} = 0, 0.14, 0.5$, and 1): open circles (respectively closed squares).

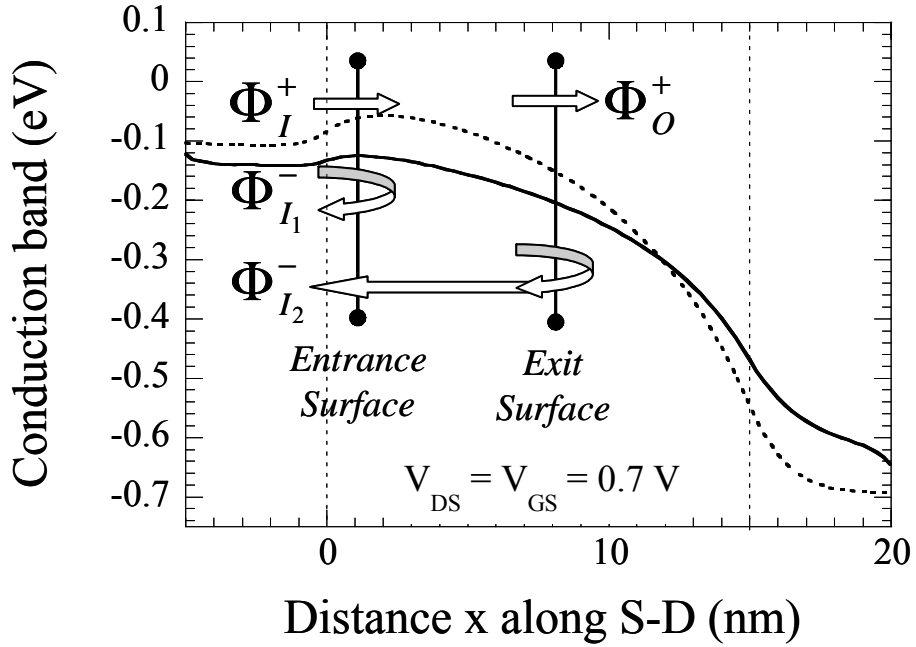


Fig. 13: Fluxes schematic and conduction band versus distance x along the S-D direction. Vertical dotted lines indicate source/channel and channel/drain junctions.

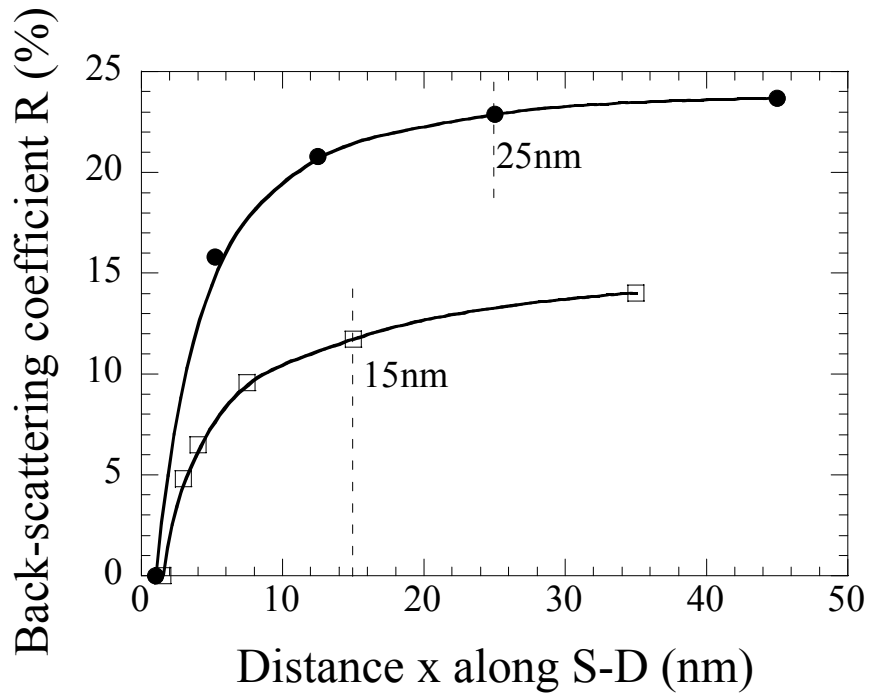


Fig. 14: Back-scattering coefficient $R(x)$ versus S-D distance x in the channel. Closed circles: $L_{ch} = 25$ nm and open squares: $L_{ch} = 15$ nm.

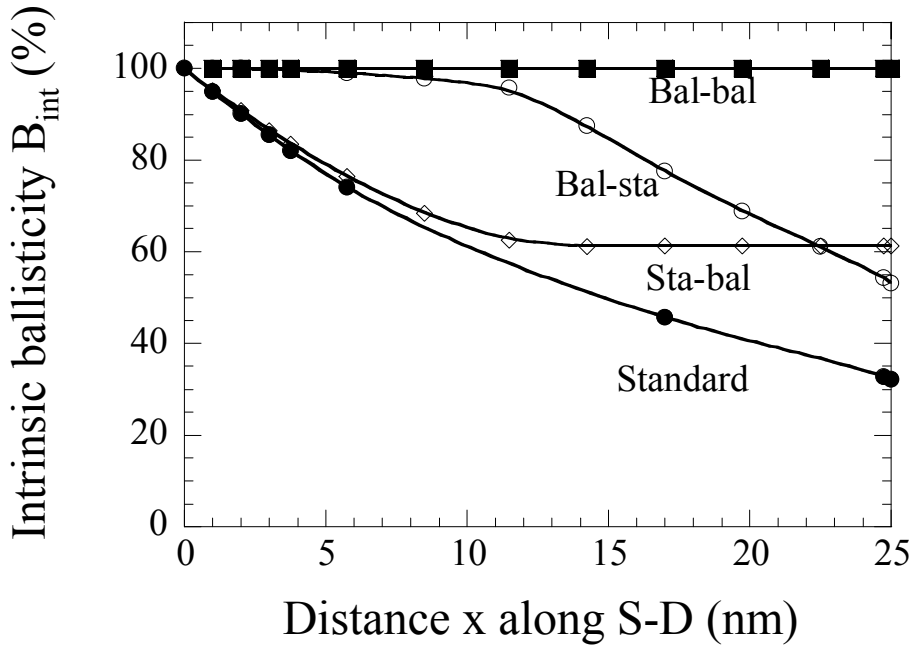


Fig. 15: Intrinsic ballisticity versus S-D distance x in the channel for devices with $L_{ch} = 25$ nm: 'standard' (closed circles), 'sta-bal' (open diamonds), 'bal-sta' (open circles), and 'bal-bal' (closed squares).

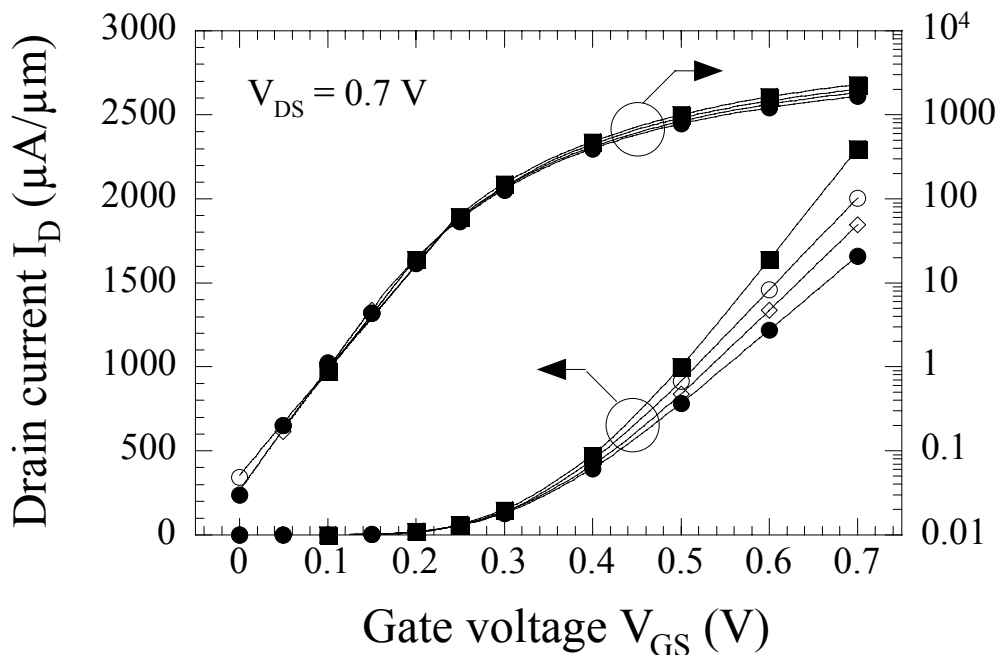


Fig. 16: I_D versus V_{GS} at $V_{DS} = 0.7$ V for different devices: 'standard' (closed circles), 'sta-bal' (open diamonds), 'bal-sta' (open circles), and 'bal-bal' (closed squares).

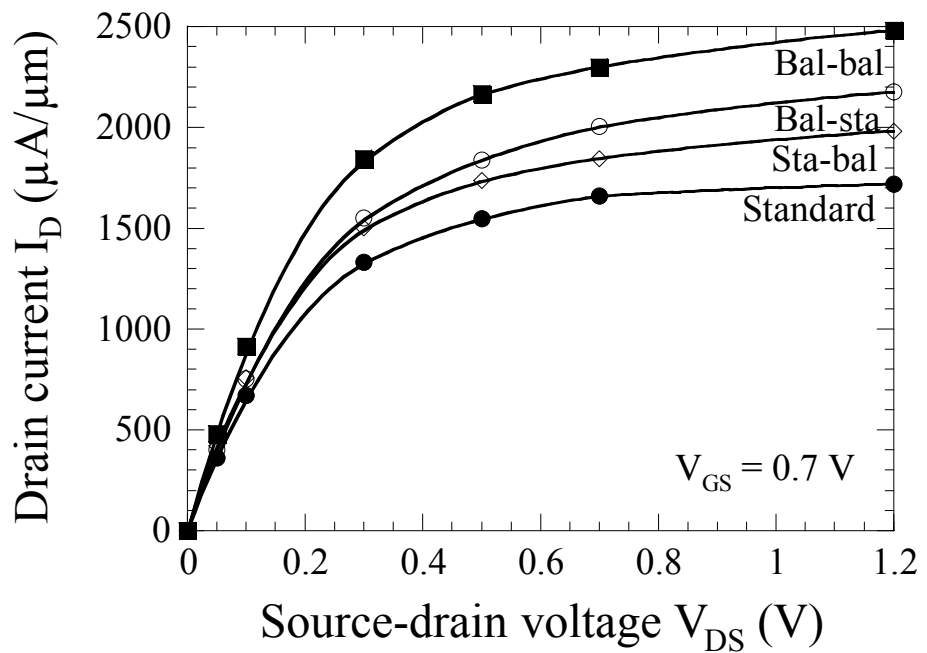


Fig. 17: I_D versus V_{DS} at $V_{GS} = 0.7$ V for the same devices as in Fig. 16.